Atmospheric Research 147–148 (2014) 86–100

Contents lists available at ScienceDirect

Atmospheric Research

journal homepage: www.elsevier.com/locate/atmos

Monitoring water phase dynamics in winter clouds

Edwin F. Campos [a,*], Randolph Ware [b,c,d], Paul Joe [e], David Hudak [e]

[a] Argonne National Laboratory, Argonne, IL, USA
[b] Radiometrics Corporation, Boulder, CO, USA
[c] National Center for Atmospheric Research, Boulder, CO, USA
[d] Cooperative Institute for Research in the Environmental Sciences, Boulder, CO, USA
[e] Meteorological Research Division, Environment Canada, Toronto, Ontario, Canada

ARTICLE INFO

Article history:
Received 29 January 2014
Received in revised form 3 March 2014
Accepted 11 March 2014
Available online 20 March 2014

Keywords:
Cloud
Microwave radiometer
Mixed phase
Supercooled droplet
Snowstorm

ABSTRACT

This work presents observations of water phase dynamics that demonstrate the theoretical Wegener–Bergeron–Findeisen concepts in mixed-phase winter storms. The work analyzes vertical profiles of air vapor pressure, and equilibrium vapor pressure over liquid water and ice. Based only on the magnitude ranking of these vapor pressures, we identified conditions where liquid droplets and ice particles grow or deplete simultaneously, as well as the conditions where droplets evaporate and ice particles grow by vapor diffusion. The method is applied to ground-based remote-sensing observations during two snowstorms, using two distinct microwave profiling radiometers operating in different climatic regions (North American Central High Plains and Great Lakes).

The results are compared with independent microwave radiometer retrievals of vertically integrated liquid water, cloud-base estimates from a co-located ceilometer, reflectivity factor and Doppler velocity observations by nearby vertically pointing radars, and radiometer estimates of liquid water layers aloft. This work thus makes a positive contribution toward monitoring and nowcasting the evolution of supercooled droplets in winter clouds.

1. Introduction

Mixed-phase clouds have a significant climate role, particularly on the surface energy budget through modulation of radiative fluxes in cold regions (e.g., Morrison et al., 2012). Radiative properties of mixed-phase clouds are determined by the distinctive microphysical properties and processes of solid and liquid cloud particles, which remain poorly understood and inaccurately represented in current numerical models (e.g., Xie et al., 2008; Tjernström et al., 2008).

Nowcasting of mixed-phase clouds is also important for weather modification (Xue et al., 2013a,b) and because it is often associated with adverse weather. Icing conditions and reduced visibility on airport runways, roads, or aircraft represent a hazard for ground and air transportation. Adverse icing and visibility conditions also compromise competition fairness during high-profile sport events such as the winter Olympics. Glaciated, liquid, and vapor water phases often coexist in each North American winter storm. Aircraft measurement analysis of winter clouds, using 3 km (30 s) samples at temperatures from 0 °C to −25 °C, found that ice and liquid cloud particles co-exist approximately 40% of the time (Cober et al., 2001, p.1992).

Dynamic exchanges among solid, liquid, and vapor phases of water describe the evolution of cloud and precipitation particles in the atmosphere. Observing these water exchanges among natural snow and cloud droplets is challenging because it requires simultaneous monitoring of distinct variables, sampled at cloud scales and at several minute intervals (at least).

* Corresponding author at: Argonne National Laboratory – CELS/EVS, 9700 South Cass Avenue, Building 240, Argonne, IL 60439, USA. Tel.: +1 630 252 0093.
E-mail address: ecampos@anl.gov (E.F. Campos).

http://dx.doi.org/10.1016/j.atmosres.2014.03.008
0169-8095/

Laboratory observations, usually involving complex experiments in controlled environments, are a way to build conceptual hypotheses about water phase exchanges in clouds. In natural clouds, however, observations by radiosondes, instrumented aircraft, or radar are insufficient to provide robust validation to these conceptual hypotheses. Radiosonde and aircraft instruments provide only point measurements for a limited number of vertical profiles, and radar observations are not sensitive to water vapor.

Microwave profiling radiometers, on the other hand, are proven tools for monitoring vertical profiles of temperature and water vapor density, as well as vertically integrated amounts of vapor and cloud droplets (water vapor and liquid water paths) at the minute and hundreds-of-meters scales (e.g., Hogg et al., 1983; Candlish et al., 2012; Sánchez et al., 2013).

Debate exists on the extent that microwave profiling radiometer can monitor vertical profiles of Liquid Water Content (LWC), which is another fundamental variable for understanding mixed-phase clouds. Theoretical arguments (Ebell et al., 2010; Crewell et al., 2009) are quick to indicate radiometry retrieval limitations due to vertical resolution (due to the vertical/range weighting functions) and sensitivity (due to insufficient independent information sources, or degrees of freedom). However, our radiometer retrievals make use of additional information, including cloud base height (temperature profile combined with cloud base height), and liquid profile shape (historical radiosonde temperature and dewpoint depression). The neural network algorithm automatically distributes integrated liquid at heights above cloud base with temperature >20 °C, in dynamic profile shapes physically linked to historical radiosondes including cloud liquid estimates (Decker et al., 1978; Solheim et al., 1998a, 1998b).

Therefore, it is observed in practice that some useful skill exist in various machine learning estimates of LWC based on observations by microwave profiling radiometer [e.g., Cimini et al., 2011; Knupp et al., 2009; Ware et al., 2003, 2013; Solheim et al., 1998a), even though the accuracy of the resulting liquid profiles is not yet rigorously determined (e.g. Solheim et al., 1998a, 1998b; Ware et al., 2003, 2013; Crewell et al., 2009; Knupp et al., 2009; Cimini et al., 2010; Serke et al., 2014).

Aside from the radiometry LWC debate, it also possible for profiling radiometer techniques to contribute significantly to the study of mixed-phase clouds, by focusing on the identification of regions favorable for developing supercooled droplets (instead of focusing only on the estimation of LWC profiles). Consequently, the following sections present a conceptual model for monitoring water-phase dynamics in clouds. The analysis method can use time series for co-located profiles of temperature and water vapor from any data source. The conceptual model is applied here, for the first time, to observations from microwave profiling radiometer in natural mixed-phase clouds. The article provides analyses and interpretation of observations during snowstorms taken by two similar radiometers placed at different climate locations. To corroborate our analyses, we compare the results of our conceptual model with an educated guess on the presence or absence of liquid water aloft, which is independently determined from the radiometer observations. We use independent cloud liquid retrievals from the microwave profiling radiometers, cloud-base estimates from a co-located ceilometer, and reflectivity factor and Doppler velocity observations by vertically pointing radars located near the radiometers.

2. Methods

2.1. Conceptual model

Consider a cloud consisting of water vapor, liquid droplets, and ice particles. The rate of condensational growth (or evaporation) of the droplets and ice particles in this mixed-phase cloud is proportional to the difference between in-cloud vapor pressure (e) and equilibrium vapor pressure over liquid water (e_s) and ice (e_i), respectively. Since at subfreezing temperatures $e_s > e_i$, there are three possible inequalities among e, e_s, and e_i (Korolev, 2007), thereby resulting in three mutually exclusive scenarios for the evolution of mixed-phase clouds:

Scenario 1: Droplet-ice growth, $e > e_s > e_i$. In this case, droplets and ice particles grow simultaneously by vapor diffusion. The liquid droplets and ice particles both compete for water vapor. This condition may occur in ascending mixed-phase clouds. It may also occur in zones of isobaric mixing.

Scenario 2: Evaporation deposition, $e_s > e > e_i$. In this case, droplets evaporate, whereas ice particles grow by vapor diffusion (deposition). This is the most widely known of the three scenarios and is often called the Wegener–Bergeron–Findeisen process (Wegener, 1911; Bergeron, 1935; Findeisen, 1938). In mixed-phase clouds, this may occur in both updrafts and downdrafts.

Scenario 3: Droplet-ice depletion, $e_s > e_i > e$. In this case, droplets and ice particles deplete simultaneously. Droplet evaporation and ice-particle sublimation may occur as a result of entrainment and mixing with environmental dry air near the cloud boundaries.

In practice, each of the e, e_s, and e_i estimates has an associated uncertainty, which can be difficult to assess. Fortunately, determination of a valid scenario can be accomplished simply by considering the statistical significance of the difference between a vapor pressure and a saturation vapor pressure. Recall that the difference between two datasets is statistically significant if it cannot be explained by chance only.

For example, the droplet-ice growth scenario can be simply identified where e is significantly larger than e_s (because $e_s > e_i$ always). The aim is then to reject the statistical null hypothesis, that $e = e_s$, in cases where the vapor pressure estimates indicate that $e > e_s$. Let us say it in other words.

$$\text{Scenario 1} \;:\; e - e_s > 0, \text{ with one-tail significance} = 0.01. \qquad (1)$$

Note that now the uncertainty of e, e_s, and e_i are irrelevant, since what we want to obtain is the uncertainty of $(e - e_s)$. In this case, a significance level of 0.01 will indicate that a positive value of $e - e_s$ has only a 1% probability of occurring by chance alone. Computation of a significance level requires knowing the probability distribution of $e - e_s$. We will assume here that this distribution is given by the Student's T probability distribution (a symmetric bell-shaped distribution, like the

normal distribution with heavier tails) for cases where e and e_s are paired (correlated) samples. (Section 3 will show that e and e_s are correlated.) In other words, we will apply here a Student's T test that two datasets have significantly different and positive means (Press et al., 2002, section 14.2, p. 618), for paired samples at 0.01 significance level (one-tailed directional test, Fig. 1). During implementation of this T-test for paired samples, at each particular time and height, we input 10 + 1 consecutive observations of the pair (e, e_s). These observations are centered at the particular height and include periods at the particular time ±5 time steps (i.e., in this case each period corresponds to a time-moving window of approximately 25 min for the MP-3000A and 5 min for the TP/WVP-3000).

The droplet-ice growth scenario is perhaps the most important for weather and climate applications because it is the scenario conducive to supercooled cloud droplets. Therefore, this is the scenario we want to identify first in a cloud. However, the presence of the other two scenarios can be monitored in a similar manner. For example, scenario 3 of droplet-ice depletion can be simply identified where e_i is significantly larger than e (because $e_s > e_i$ always). The aim here will then be to reject the statistical null hypothesis, that $e_i = e$, in cases where the vapor pressure estimates indicate that $e_i > e$. Let us say it in other words.

$$\text{Scenario 3} : e_i - e > 0, \text{ with one-tail significance} = 0.01. \quad (2)$$

Similarly, we can say the following.

$$\text{Scenario 2} : (e_s - e > 0) \text{ and } (e - e_i > 0), \text{ both with one-tail significance} = 0.01. \quad (3)$$

The implementation of our conceptual model simply requires as input the time series for co-located profiles of temperature and vapor density. The air vapor pressure (e, in hPa) is obtained here from (e.g., Rogers and Yau, 1991, p. 12)

$$e = \rho_v R_v T \times 10^{-5}, \quad (4)$$

where ρ_v is the air vapor density (in g m^{-3}), T is the temperature (in Kelvins), and $R_v = 461.5$ m^2 s^{-2} K^{-1} is the gas constant for water vapor. For obtaining the saturation vapor pressure over ice (e_i, in hPa) and the saturation vapor pressure over liquid water (e_s, in hPa), the following equations are used (Murphy and Koop, 2005, Eqs. (7) and (10), respectively):

$$e_i = 10^{-2} \times \exp\left[a_0 + \frac{a_1}{T} + a_2 \ln(T) + a_3 T\right], \quad (5)$$

$$e_s = 10^{-2} \times \exp\left\{a_0 + \frac{a_1}{T} + a_2 \ln(T) + a_3 T + (\tanh[a_4(T + a_5)])\right) \times \left[a_6 + \frac{a_7}{T} + a_8 \ln(T) + a_9 T\right]\right\}, \quad (6)$$

where a_i (with i varying from 0 to 9) corresponds to the empirical coefficients in Table 1. Note that Eq. (5) is valid for 273.15 K > T > 110 K (or 0 °C > T > −163.15 °C), and Eq. (6) is valid for T between 123 and 332 K (or −150.15 and 58.85 °C).

In summary, this conceptual model is based only on the magnitude ranking of in-cloud vapor pressures and equilibrium vapor pressures over liquid water and over ice. This should be enough to identify the conditions where liquid droplets and ice particles grow or deplete simultaneously, as well as the conditions where droplets evaporate and ice particles grow by deposition from vapor diffusion.

2.2. Experimental setup

Two snowstorm examples are presented, the first corresponds to a winter lake-effect event that occurred on 23 February 2006 at the Environment Canada Centre for Atmospheric Research Experiments (CARE, located about 80 km N of Toronto, in Ontario, Canada). For this event, precipitation was observed at ground level in the form of melting snow, starting around 16 UTC and finishing by 2230 UTC. For these analyses, measurements from a 12-channel microwave profiling radiometer (Radiometrics model TP/WVP-3000) were used. It was located at 44.23°N, 79.78°W, and 249 m above sea level. In addition, a ceilometer and an X-band vertically pointing radar provided co-located complementary observations of this snowstorm.

The second example is a winter upslope snowstorm that occurred on 14 February 2008 at Boulder (Colorado, USA). For this event, precipitation was observed at the ground in the form of powder (low-density, fluffy, and dry particles) snow, for a period roughly between 09 and 18 UTC. For these analyses, 22-channel measurements from a microwave profiling radiometer (Radiometrics model MP-3000A) were

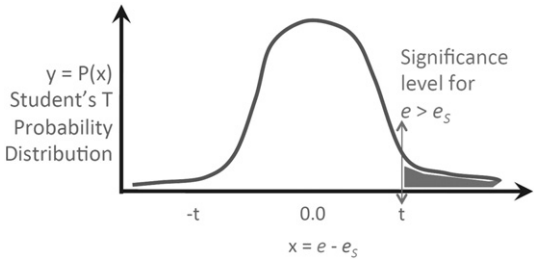

Fig. 1. One-tailed directional test that two datasets, e and e_s, have significantly different and positive means. This uses a hypothetical Student's T probability distribution for paired samples and $t = 0.01$ significance level.

Table 1
Empirical coefficients for computing saturation vapor pressure over ice (e_i) and over liquid water (e_s). Values are from Murphy and Koop (2005, Eqs. (7) and (10)).

Coefficient	For e_i use in Eq. (5)	For e_s use in Eq. (6)
a_0	9.550426	54.842763
a_1	−5723.265	−6763.22
a_2	3.53068	−4.210
a_3	−0.00728332	0.000367
a_4		0.0415
a_5		−218.8
a_6		53.878
a_7		−1331.22
a_8		−9.44523
a_9		0.014025

used. It was located at 40.01°N, 105.15°W, and 1616 m above sea level. In addition, a UHF-band vertically pointing radar provided co-located complementary observations of this snowstorm.

2.3. Radiometer sensors

The radiometer's accuracy and high temporal resolution (1 min), coupled with its water vapor and liquid water profiling capabilities, make this instrument a convenient platform to study water phase changes inherent in snowstorms.

The radiometer observes atmospheric microwave (K band at 22–30 GHz and V band at 51–59 GHz) and infrared (9.6–11.5 μm) emissions along with surface temperature, humidity, and pressure. Table 2 lists the particular channels where microwave emissions are taken. Every minute, the radiometer software converts these observations into vertically-integrated water vapor and liquid water amounts (i.e., water vapor paths and liquid water paths aloft), as well as vertical profiles of air temperature, relative humidity, water vapor content (density), and liquid water content (density). Each profile is retrieved independently by using a neural network algorithm (Solheim et al., 1998a, 1998b) trained by forward modeling many years of historical operational radiosonde data with a radiative transfer model (Rosenkranz, 1998). The proprietary software in the radiometer control computer generates these retrievals. The vertical spacing in each retrieved profile is 100 m for 0–2 km height for the TP/WVP-3000, 50 m for 0–0.5 km height and 100 m for 0.5–2 km for the MP-3000A, and 250 m from 2 to 10 km height for both instruments. The retrieval vertical spacing is actually finer than the radiometer vertical resolution. Temperature profiles have a vertical resolution of 100 m in the first 500 m, degrading rapidly to 500 m and to 1 km in the first kilometer. Humidity profiles have a much coarser vertical resolution of about 500 m decreasing to 1 km in the first kilometer and decreasing further at increasing heights (e.g., Westwater et al., 2000; Cadeddu et al., 2002, 2009, 2013; Liljegren et al., 2005; Hewison, 2007).

The retrieval output is not only statistical; it also integrates physical information. For example, the cloud-base height, estimated by combining the zenith infrared measurement of cloud-base brightness temperature and the retrieved air-temperature profile, places a strong, independent constraint on the humidity profile (at cloud base, it must be saturated with respect to liquid). The sensitivity of profiling radiometer retrievals in low vapor and liquid water conditions is discussed by Cimini et al. (2007, 2010).

Estimation and improvement of the accuracy in radiometer retrievals have a long history. We present a summary in the Appendix A citing only a few representative works.

Our radiometer detectability threshold for liquid water content estimates is an educated guess of the presence or absence of liquid water aloft. The threshold is obtained from the cumulative probability distribution of liquid water contents. Fig. 2 depicts a hypothetical cumulative probability distribution of liquid water contents, obtained from radiometer observations (as explained in the previous paragraph). Let us then propose that two regimes exist in the cumulative distribution, which are differentiated by a major slope change in the distribution curve. From the minimum liquid water content to the main inflection point (in the x axis), the estimated liquid amounts are all associated to random errors of the neural network algorithm. Between the main inflection point and the maximum liquid water contents (in the x axis), the estimated liquid amounts are associated with real liquid water particles detected by the radiometer. Therefore, for a positive comparison with our conceptual model, we will look for agreement between the droplet-ice growth scenario and (time-height) regions where the liquid water content is above the radiometer detectability threshold.

2.4. Other sensors

Vertically pointing Doppler radars, co-located with the radiometers, provided complementary observations for this study, which allowed qualitative validation of the radiometer retrievals. The McGill Vertically Pointing Doppler Radar (VPDR) was used for the winter lake-effect event (on 23 February 2006). This is an X-band (9.35 GHz) radar, operated by McGill University; it is described by Zawadzki et al. (2001). By comparison with co-located ground sensors, we estimate that this radar was able to detect snow at lower heights only for intensities greater than about 0.02 mm h^{-1} (melted-equivalent snowfall rate).

The NCAR-ISS wind profiler was used for the winter upslope event (on 14 February 2008). This is a vertically pointing Doppler radar, operated by NCAR Foothills Laboratory, and is located 1 km north of the radiometer site. This UHF-band (915 MHz) radar wind profiler is described by Parsons et al. (1994, and references therein). This radar was

Table 2
Frequency channels where our profiling radiometers measure microwave brightness temperature. The ones in bold are used for meteorological profile retrievals.

	MP-3000A radiometer	TP/WVP-3000 radiometer
K-band channels (GHz)	22.0, **22.234**, **22.5**, 23.0, **23.034**, 23.5, **23.834**, 24.0, 24.5, **25.0**, 25.5, 26.0, **26.234**, 26.5, 27.0, 27.5, **28.0**, 28.5, 29.0, 29.5, **30.0**	**22.235**, **23.035**, **23.835**, **26.235**, **30.0**
V-band channels (GHz)	**51.248**, **51.76**, **52.28**, **52.804**, **53.336**, **53.848**, **54.4**, **54.94**, **55.5**, **56.02**, **56.66**, **57.288**, **57.964**, **58.8**	**51.25**, **52.28**, **53.85**, **54.94**, **56.66**, **57.29**, **58.8**

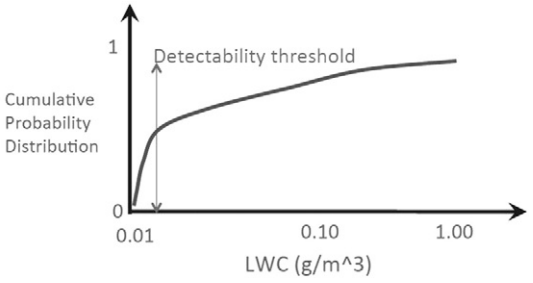

Fig. 2. Hypothetical cumulative probability distribution for radiometer estimates of liquid water content at various times and heights above the radiometer.

calibrated to provide radar reflectivity factors with accuracies in the order of 5 dB (Brown, 2008, personal communication).

Further details on these radars are given in Table 3. In addition, during the lake-effect snowstorm in Canada, a Vaisala CT25K ceilometer was co-located with the radiometer. Its cloud-base estimates provide independent validation for the liquid water content retrievals from the radiometer.

3. Results

3.1. Lake-effect snowstorm

Lake-effect snowstorms are winter weather patterns common along the lee shores of the North American Great Lakes. During this type of snowstorm, cold-air masses transport flow over the warmer surface of a North American Great Lake, resulting in cloud formation and large snowfall amounts to the lee side of the lakes. Extensive literature is available on the climatological and synoptic contexts where these storms evolve (e.g., Liu and Moore, 2004, and references therein). Potential-temperature analyses from aircraft observations indicate that lake-effect snowstorms are characterized by a well-mixed boundary layer, above which the atmosphere is stably stratified (e.g., Agee and Gilbert, 1989).

Concentrating here on the cloud-scale context, Fig. 3 presents radiometer observations of a winter lake-effect snowstorm on 23 Feb 2006 at the CARE site (Ontario, Canada). The first two panels (a and b) correspond to retrieved time-height cross sections of air temperature (in Celsius) and vapor density (in g m^{-3}), all according to the linear color scales on the corresponding right. The y axes give the height in km above the ground. The time series in panel c presents retrievals of vertically-integrated water vapor (WVpath, black line, as in the left y axis) and liquid water (LWpath, red line, as in the right y axis) in the column of atmosphere above the radiometer, both expressed in kg m^{-2}. The x axes correspond to the UTC time. Considering that there were clear-sky conditions from 00 to 07 UTC (see ceilometer observations in Fig. 4a, red crosses), we recognize that a bias in the order of 50–100 g m^{-2} exists in these liquid water paths (bottom panel) during this day. The temperature plot (top panel) shows a horizontally stratified field for heights above 1 km. A temperature inversion below 1 km height is also observed during the period before 1409 UTC. Note also that the zero Celsius isoline is above the ground level between 16 and 22 UTC. Considering that snow melts at heights just below the 0 °C isotherm level (i.e., when the air is at zero Celsius in wet-bulb temperature), melting snow is likely to be found at ground level. In the middle panel, observe the period of increase in vapor density between 13 and 19 UTC and the period of decrease in vapor density between 19 and 23 UTC. These patterns are also present in the water vapor paths of the bottom panel. The last period of water vapor depletion is matched by the presence of liquid water (see the sudden increases in LWpath in the bottom panel). The following question arises: Is this cloud liquid water (detected between 19 and 23 UTC, 23 Feb 2006) responsible for the observed depletion in water vapor density?

Probably not entirely, exclusively, because significant precipitation particles entered the sampling volume during this period (see later the evidence of this from the X-band radar observations in Fig. 6). This precipitation (in the order of 20 dBZ) can cause most of the water vapor depletion, as observed by the radiometer. However, we believe that the cloud liquid water also plays a role, and we need to examine this event more in detail.

To address this question further, Fig. 4 gives various independent and complementary analyses. The Fig. 4b provides a vapor-pressure classification for the entire event. In this panel, the green regions correspond to the droplet-ice growth scenario, the yellow indicate regions where the evaporation deposition scenario occurs [for our purposes, it only serves as an envelope around the droplet-ice growth region, i.e. around the green regions that can serve as basis for supercooled water forecasts; see also Eq. (1)], and the red corresponds to the droplet-ice depletion scenario. The white regions (labeled as "other") correspond to conditions where $T > 0$ °C, $e_s = e_i$, $e_s = e$, or $e_i = e$. Note the black contour inside the green region, which corresponds to the 1% significance level for $e_s - e > 0$ (i.e., Eq. (2)). In other words, this contour gives the 99% confidence level for a region allowing growth of droplet and ice particles. Similarly, the 99% confidence level for the droplet-ice depletion (red region) scenario is also included. Confidence level for the evaporation-deposition scenario (yellow region) is omitted for the sake of clarity. Recall that these significance levels are based on the Student's T test for significantly different means of paired samples, as explained in Section 2.1. We use the test of *paired* samples because the vapor pressures (e, e_s, and e_i) are correlated. Even though this correlation is expected, since the vapor pressures depend strongly on the same radiometer temperature retrievals (Eqs. (4), (5), and (6)), we verify it by computing the corresponding linear Pearson correlation coefficients (Neter et al., 1988) in Table 4.

The Fig. 4a corresponds to our estimate on the presence or absence of liquid water aloft. It is based on a radiometer detectability threshold of 0.060 g m^{-3}, determined from Fig. 5a. This threshold is the minimum discernible amount of liquid water content from our radiometer observations; it is obtained from the inflection point (slope change) in the corresponding cumulative probability distribution (as explained in last paragraph of Section 2.3). [The threshold estimation is independent of the method used to obtain the cumulative probability distribution. Fig. 5, for example, uses two different methods. The first method is plotted in black, and its x axis uses extremely small bin sizes (0.0001 g m^{-3}). The second method is plotted in red, and it optimizes the distribution bin sizes using a kernel density estimator by Botev et al. (2010).]

In Fig. 4a, note the indication of cloud droplets at heights roughly below 3.5 km (discernible liquid water contents). This

Table 3
Parameters of vertically pointing radars.

	X-band McGill VPDR	*UHF-band NCAR ISS*
Wavelength (frequency)	3.2 cm (9.35 GHz)	32.8 cm (915 MHz)
Pulse length	150 m	100 m and 400 m
Beam width (one way)	2°	9°
Peak transmitted power	25 kW	500 W
Pulse-repetition period	769 μs	50 μs and 100 μs
Minimum detectable precipitation	~0.01 mm/h	~1 mm/h

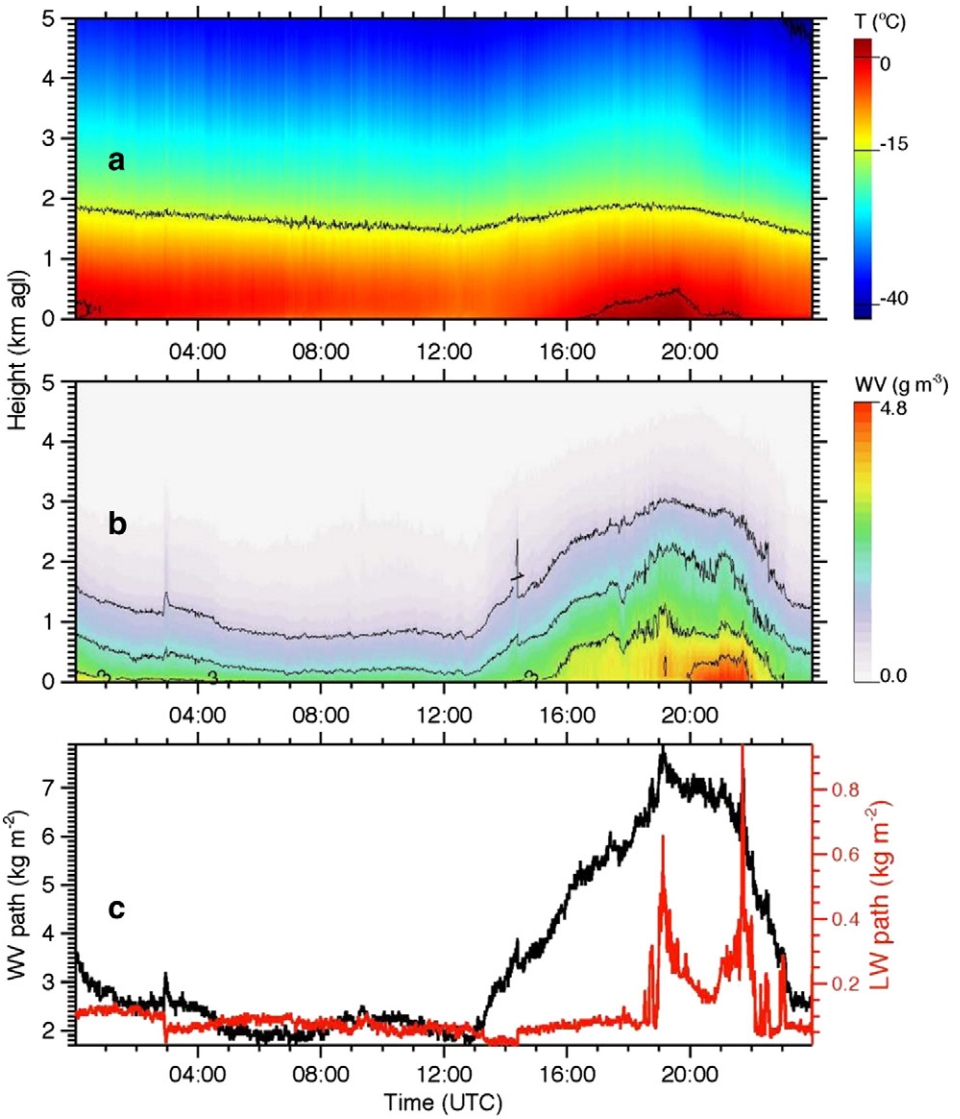

Fig. 3. Microwave profiling-radiometer retrievals of a winter lake-effect snowstorm (North American Great Lakes), on 23 Feb 2006 at 80 km north of Toronto, Ontario (Canada).

liquid water is supercooled, because it is present in regions of the atmosphere where the temperature is below freezing (see Fig. 3a). During this event, melting snow was observed at ground between 1930 and 22 UTC. Solid and liquid water phases were present between 19 and 22 UTC. If droplet-ice growth conditions existed, then the source of the growth must be the available water vapor. In Fig. 4b, the droplet-ice growth scenario is observed at 17–22 UTC, for heights above 1 km and below 3.5 km, roughly. In agreement, the liquid water is discernible within similar period and heights (Fig. 4a). Note, however, that the droplet-ice growth scenario (green region in Fig. 4b) corresponds to conditions *favorable to develop* supercooled liquid water, whereas the discernible liquid water estimates (green region in Fig. 4a) corresponds to conditions *with developed* supercooled liquid water.

The cross and x symbols plotted in Fig. 4a correspond to cloud-base estimates from the co-located ceilometer. The black x symbols are estimates for the lowest cloud bases; but for this event, the ceilometer algorithms are wrongly interpreting blowing snow signals as clouds. The red crosses, however, correspond to ceilometer estimates of the second lowest cloud bases, and we will focus on these. For the period between 16 and 24 UTC, these cloud-base estimates are in general agreement with the ice-droplet growth scenario and the discernible liquid water regions in the figure. The agreement exception is in the elevated cloud base above 3.5 km heights around 7–12 UTC. This is an expected disagreement for ice-only clouds, and we will show that this is the case here, by analyzing co-located radar observations.

A more detailed analysis is possible by identifying the vertical distribution of precipitation particles. Fig. 6 presents observations by the X-band vertically pointing radar during the same snowstorm. The Fig. 6a corresponds to time-height cross sections of radar reflectivity factor (in dBZ, according to

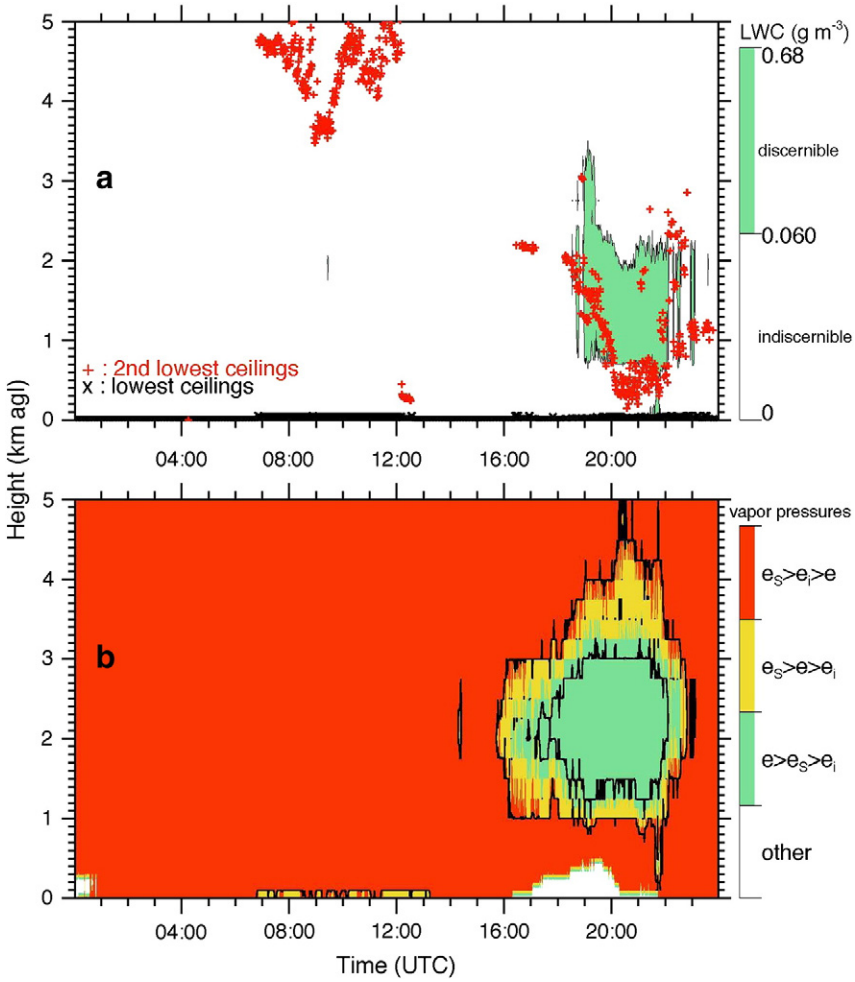

Fig. 4. Liquid-water detection (a) and vapor-pressure class (b) estimated by the microwave profiling radiometer for the winter lake-effect snowstorm on 23 Feb 2006 at Ontario. The y axes give heights in km above the ground level, and the x axes give the UTC time. The corresponding color scales are given at the right of each panel.

the color scale in the left center), and the Fig. 6b corresponds to time-height cross sections of vertical Doppler velocity (in m s^{-1}, negative downwards, according to the color scale in the right center). In both cases, the y axis corresponds to height in km above the ground level and the x axis to UTC time. Precipitation features are evident here for the snowstorm discussed in the previous paragraphs.

Table 4
Linear Pearson correlation coefficients for corresponding radiometer estimates of vapor pressure (e), saturation vapor pressure over liquid water (e_s), and saturation vapor pressure over ice (e_i).

Period	e and e_s correlations	e and e_i correlations
0000–1244 UTC, 2006 Feb 23 Lake-effect snowstorm before transition	0.92	0.92
1245–2400 UTC, 2006 Feb 23 Lake-effect snowstorm after transition	0.96	0.95
0200–0414 UTC, 2008 Feb 14 Upslope snowstorm before transition	0.89	0.94
0415–1000 UTC, 2008 Feb 14 Upslope snowstorm after transition	0.91	0.92

For the precipitation patch between 19 and 24 UTC, at heights below 6.5 km, Fig. 6a indicates significant reflectivity increase (more and or larger precipitation particles) around 3 km height, which coincides with the Droplet-ice growth scenario determined in Fig. 4b. Also for this period, some Doppler fall velocities are larger than 2 m s^{-1} (blue pixels in Fig. 6b), which are too fast for dry snowflakes targets. However, these Doppler velocities can be explained as rimed-snow radar targets (denser particles that fall a bit faster than 2 m s^{-1}). Therefore, this is indirect evidence of supercooled liquid water (the droplets riming the snow), in rough agreement with the radiometer liquid water estimates and scenarios of Fig. 4. Note that good agreement has already been reported between cloud liquid profiles measured by balloon-borne supercooled liquid sensors and an MP-3000A radiometer (Serke et al., 2014).

In addition, the period around 19–20 UTC is characterized by WV depletion (Fig. 3b and c). This depletion can be due to

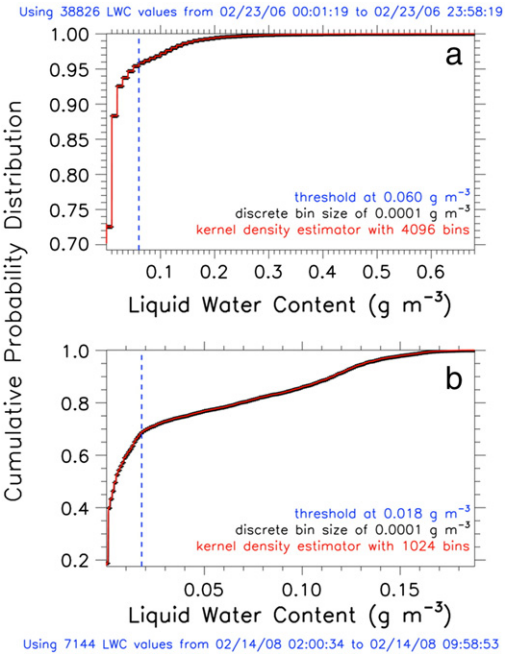

Fig. 5. Detectability thresholds for liquid water above microwave profiling radiometers. The threshold is the minimum discernible amount of liquid water content (Figs. 4a and 8a). The panel a (0.060 g m^{-3} threshold using the TP/WVP-3000 12-channel radiometer) corresponds to the winter lake-effect snowstorm at Ontario (Canada) on 23 Feb 2006. The panel b (0.018 g m−3 threshold using the MP-3000A 22-channel radiometer) corresponds to the winter upslope snowstorm at Colorado (USA) on 14 Feb 2008. The plots indicate (in blue) the number of liquid water content (LWC) points used for each threshold estimate.

the entering of a cold and dry air mass, as well as by an increase in ice crystals (the Wegener–Bergeron–Findeisen processes) coming from outside the sampling volume. The low reflectivity echoes registered by radar that do not match with discernible LWC contours recorded by the radiometer are areas where ice phase clouds predominate, and where it is occurring WV depletion.

For the precipitation patch between 07 and 12 UTC, at heights between 3 and 6 km, the Fig. 6b indicates that these are snow particles, because reflectivity factors are around zero dBZ and Doppler fall velocities are between zero and 2 m s^{-1}. This is in agreement with the analyses in Fig. 4a, where the ceilometer indicates a cloud-base above 3.4 km for this period, and the radiometer indicates absence of discernible liquid water in this cloud. The vapor pressure conditions also indicate evaporation and sublimation (droplet-ice depletion conditions in Fig. 4b). The radar observations are then consistent with the radiometer and ceilometer estimates.

3.2. Winter upslope snowstorm

Climatology and dynamics of winter upslope snowstorms, along the eastern margin of the Colorado Rockies, are well understood at the synoptic scale (e.g., Dunn, 1987; Mahoney et al., 1995). Concentrating here on the cloud scale, Fig. 7 shows radiometer observations for the onset and development of a winter upslope snowstorm, on 14 February 2008 at Boulder. The top and middle panels in this figure correspond to vertical profiles of air temperature and vapor density, respectively. The bottom panel shows retrievals of vertically integrated water vapor (WV path, black line, as in the left y axis) and cloud liquid (LWpath, red line, as in the right y axis), both expressed in kg m^{-2}.

In all panels of Figs. 7 and 8, the periods after 0836 UTC (hereafter, all times are read directly from the radiometer Level2 output files, which have a time resolution of one minute) are filled with black vertical lines to indicate the presence of liquid water on the radiometer rain sensor. In other words, the precipitation began at 0836 UTC for this event. (In this case, the rain sensor wets mainly because snow melts on the warm radiometer structure). The impact of a small amount of liquid water on the radome is negligible on the retrieved profiles, as seen by the consistent retrievals before and after 0836 UTC. We discard the possibility that the neural network retrievals would give mean conditions during wet radiometer periods, because the mean conditions would look more like before the frontal passage (i.e. before 4:15 UTC), which is not the observed case here. During heavy rain (not our cases), zenith brightness temperature measurements can saturate (approach ambient temperature), causing instability in the neural network retrievals. Then, large positive bias will appear in the retrieved atmospheric profiles. In addition to saturation, heavy rain significantly scatters the atmospheric microwave emissions, and this additional scattering signal is not considered in any radiometry retrieval algorithm. In order to reduce these inconveniences, off-zenith sampling methods have been used to obtain stable retrievals during heavy rain (Cimini et al., 2011; Ware et al., 2013; Raju et al., 2013; Xu et al., 2014). Positive error resulting from ice accrual during freezing rain that occurs on the top and the windward side of the radiometer radome can be minimized using off-zenith observations on the lee side of the radiometer radome (e.g., Ware et al., 2013). For the cases analyzed in this study, however, off-zenith sampling methods were not needed.

Fig. 7a shows a cold front that arrived at the radiometer site around 0415 UTC. The retrieved profiles show the sharp drop in temperature and rise in vapor density (Fig. 7b) that occurred below 3 km height. By definition, the frontal boundary around 0415 UTC implies strong advection of a different air mass into the radiometer sampling volume, and it complicates the analyses of cloud water-phase dynamics for this event. The increase of vapor density that follows the frontal passage (Fig. 7b) is due primarily to advection. After that, we can assume that local microphysical processes are driving the water-phase dynamics. Characterization of our three theoretical scenarios (droplet-ice growth, evaporation deposition, and droplet-ice depletion), in combination with radar observations, allows a reasonable qualitative analysis of the situation.

At about 06 UTC, the water vapor path starts to decrease when the liquid water path increases (Fig. 7c). Condensation of cloud liquid appears to deplete the water vapor density. However, the following questions arise: (1) Why is cloud liquid water not observed in the period between 0430 and 06 UTC (i.e., right after the front passes over the radiometer site)? and (2) What makes the cloud liquid water disappear after about 0930 UTC?

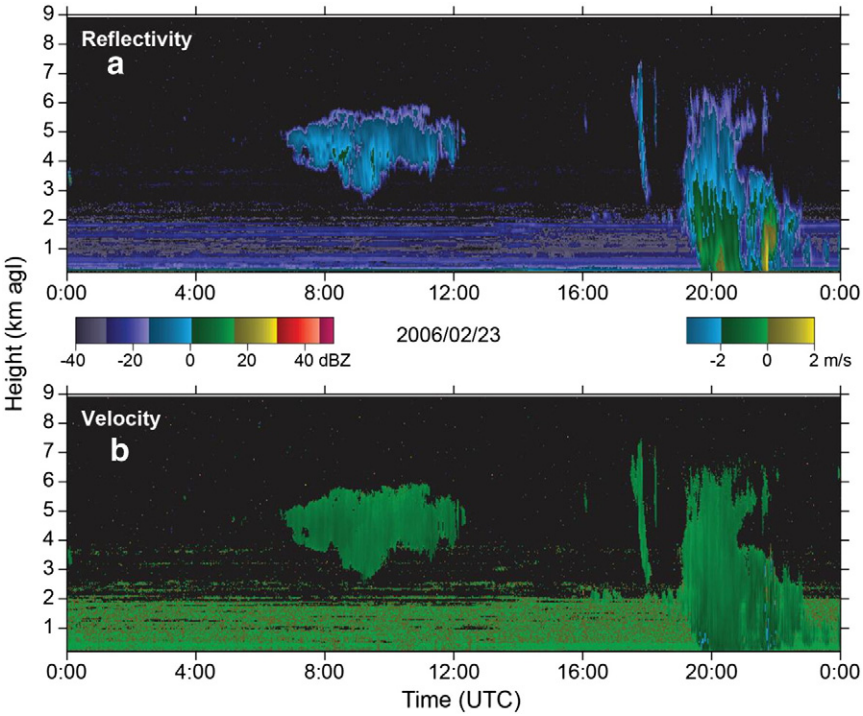

Fig. 6. X-band vertically pointing radar observations of a winter lake-effect snowstorm (North American Great Lakes), on 23 Feb 2006 at 80 km north of Toronto, Ontario (Canada). Image courtesy of Prof. Frédéric Fabry (McGill University, Marshall Radar Observatory).

As before, we address these questions by analyzing plots of vapor-pressure classification and estimates on the presence of cloud liquid water aloft. In Fig. 8, the y axes give heights in km above the ground level, and the x axes give the UTC time. The corresponding color scales are given at the right of each panel. In Fig. 8a, the green region corresponds to observations with discernible liquid water (i.e., liquid water contents are above the detectability threshold of 0.018 g m^{-3}, as determined from Fig. 5b). In Fig. 8b, the black contours correspond to the 99% confidence level for the droplet-ice depletion (red region) and for the droplet-ice growth (green region) scenarios. Confidence level for the evaporation-deposition scenario (yellow region) is omitted for the sake of clarity.

The period between 06 and 0930 UTC corresponds to droplet-ice growth (Fig. 8b). This agrees with the liquid water paths indicated in Fig. 7c and with the discernible liquid water contents in Fig. 8a. The Fig. 7a indicates that this cloud liquid water is supercooled (between 0 °C and −15 °C). Conversely, the period between 0440 and 06 UTC and the one after 0930 UTC have regions of droplet-ice growth (Fig. 8b), but radiometer observations do not indicate cloud liquid water within these periods (Fig. 7c; as before, all times are obtained from the radiometer Level2 output files, with a 1 min resolution).

Excluding the possibility of radiometer bias errors, analyses during the first period (between 0430 and 06 UTC) can be explained by conditions where haze droplets (too small to be detected by the radiometer) are growing toward cloud-droplet sizes (detectable by the radiometer). This corresponds to the microphysical processes of aerosol nucleation (from vapor to unstable liquid water) and droplet activation (from haze to cloud). Kohler-curve theory (e.g., Rogers and Yau, 1991, p. 88) explains that the time it takes for a particle to grow from haze to droplet size will depend on factors such as haze chemical composition, rate of supersaturation increase, atmospheric temperature, and pressure. Haze droplets are unstable in the sense that its growth requires a continuous increase in supersaturation (not just supersaturation). Cloud droplets are more stable in the sense that its growth does not need an increasing supersaturation. Then, for environments where supersaturation (with respect to liquid) increase is slow, intermittent, or negative (subsaturation), one can reasonably expect that a haze population can develop to (radiometer detectable) cloud-droplet sizes in about an hour or so.

Furthermore, recall that for a haze particle to grow into a cloud particle, it is not sufficient to have $e > e_s$ but rather to have reached a critical radius within a critical equilibrium supersaturation. Haze critical radii are on the order of 1 μm, and the equilibrium supersaturation $[(e/e_s) - 1]$ is on the order of 10^{-3} or smaller (Pruppacher and Klett, 1997, p. 176). With these considerations, and based on haze droplet-size distributions measured at ground (Gultepe et al., 2009, Fig. 11, green curve for diameters of 1.7 μm or less), we estimate that haze liquid water contents are in the order of 7×10^{-5} g m^{-3}. This magnitude is much smaller than the radiometer detectability threshold (0.018 g m^{-3}, as in Fig. 5b). Therefore, liquid water contents from haze are indiscernible by the radiometer.

Therefore, for the observations on 14 Feb 2008, we believe that it is only after 06 UTC that the droplets are large enough (in number and size) to be detected by the radiometer

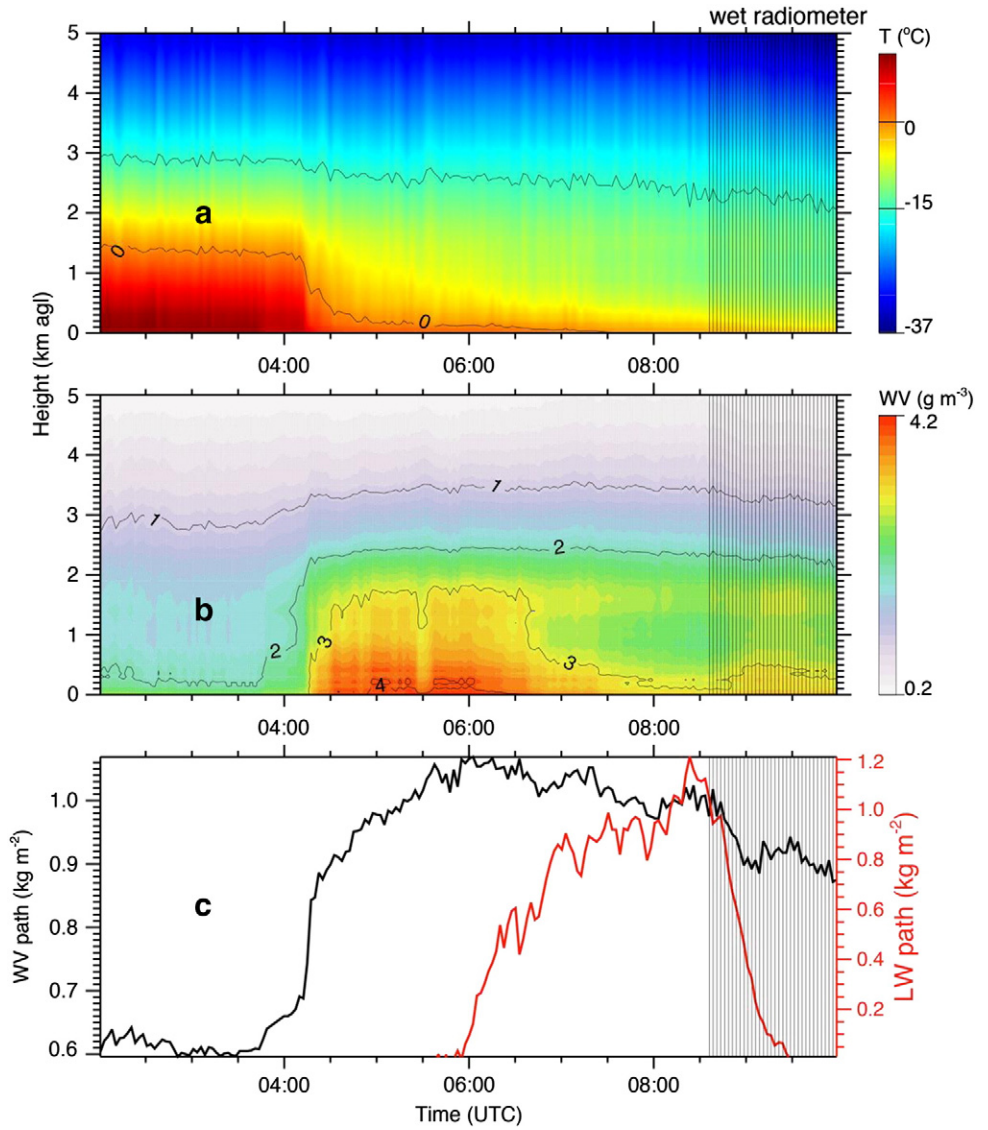

Fig. 7. Microwave profiling radiometer retrievals of a winter upslope snowstorm (North American Central High Plains) at Boulder, Colorado (USA), on 14 Feb 2008. Panel descriptions are as in Fig. 3. Black vertical lines indicate a wet radiometer (in this case, snow is melting on its warm rain sensor).

(Fig. 7c). The same reason explains why the droplet-ice growth scenario appears much earlier than the discernible amounts of liquid water content (Figs. 4a and 8a). The positive outcome is that our analysis of vapor-pressure classes (Figs. 4b and 8b) are providing more than one-hour lead time in the forecasting of supercooled liquid water.

Further analysis of the entire event is possible by using co-located observations from vertically pointing radar. Fig. 9 presents observations by a UHF-band wind profiler during the same snowstorm. The Fig. 9a corresponds to a time-height cross section of radar reflectivity factor (in dBZ), and the Fig. 9b corresponds to a time-height cross section of vertical Doppler velocity (in m s^{-1}, positive downwards), both according to the color scale on the right. The y axis corresponds to height in km above the ground level, and the x axis to UTC time. The period before 07 UTC is characterized by updrafts (negative Doppler velocities in Fig. 9b). This ascending air is responsible for transporting new amounts of water vapor aloft (vapor density increasing in Fig. 7b and water vapor path increasing in Fig. 7c). The radar signals detected during this period are actually from clear-air targets (i.e., from sharp discontinuities in the index of refraction, an index that depends on air temperature, vapor pressure and air pressure; e.g., Röttger and Larsen, 1990). These targets can be detected at the UHF band but not the X band. For example, the sharp spatial gradients of temperature and vapor pressure retrieved by the radiometer at 0415 UTC in Fig. 7 (due to the frontal passage over the radiometer site) are matched by sharp UHF reflectivity values right after 0415 UTC (Fig. 9).

For the period roughly after 07 UTC and just before 0930 UTC, the Fig. 9b indicates the appearance of precipitation,

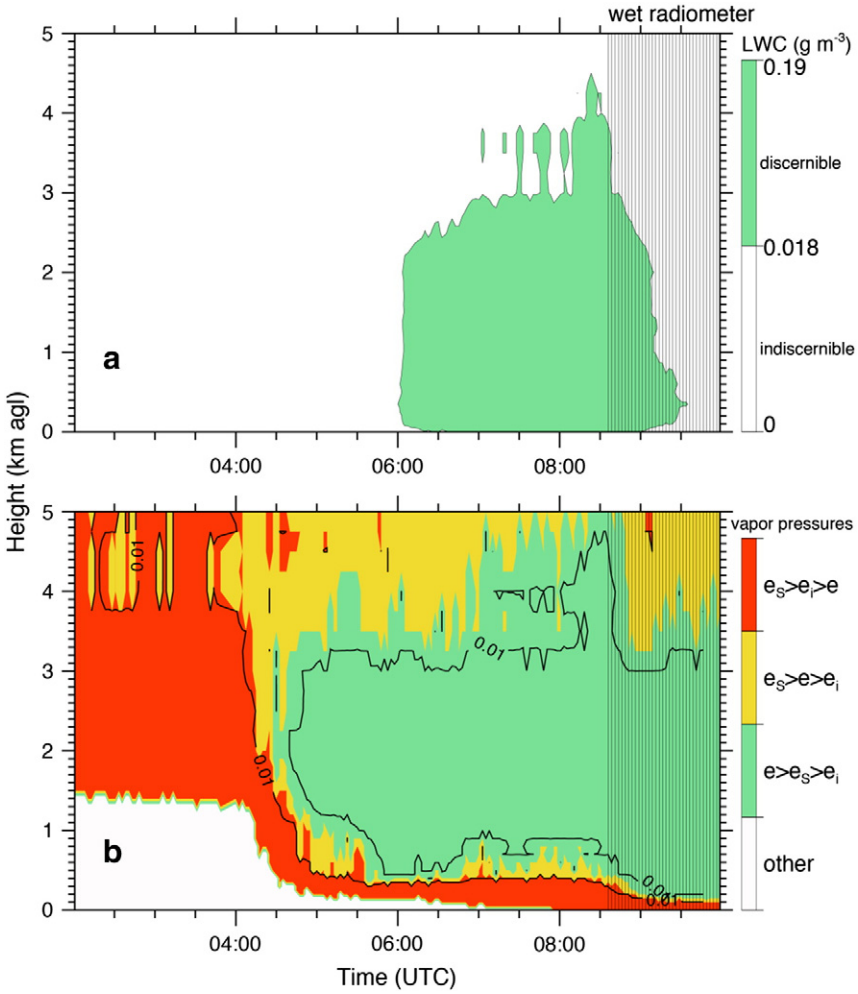

Fig. 8. Liquid-water detection (top) and vapor-pressure class (bottom) estimated by the microwave profiling radiometer for the winter upslope snowstorm on 14 Feb 2008 at Colorado. Black vertical lines indicate a wet radiometer (in this case, snow is melting on its warm rain sensor).

with Doppler vertical velocities larger than 2 m s^{-1} (downwards). After 0830 UTC, Doppler vertical velocities below 1.5 km height are even larger than 3 m s^{-1}. These magnitudes are typical fall velocities for riming snow and small raindrops (diameters around 0.8 mm; e.g., Gunn and Kinzer, 1949). Rimed snow implies the presence of cloud droplets. Thus, the UHF radar observations agree during this period with our radiometer estimates on the presence of liquid water (*i.e.*, liquid water paths in Fig. 7c, droplet-ice growth scenario in Fig. 8b, and discernible liquid water in Fig. 8a). All these suggest that, for the period roughly after 0830 UTC, supercooled droplets are being captured by snow particles during riming, right from its first formation at levels above the 2 km.

Notice also in Fig. 9a the radar echoes with reflectivity factors larger than 10 dBZ. These echoes reach above 2 km height only after about 0840 UTC. This is consistent with the evaporation deposition scenario that appears approximately after 0840 UTC and roughly above 3.5 km height (Fig. 8b), where ice and snow should grow by vapor deposition, and the liquid water should deplete. In other words, $e_s > e$ at the heights where droplets previously were starting to form, and any droplets existing there must evaporate after that time.

To answer the second question of why the observed liquid water disappeared after about 0930 UTC, let us summarize our analyses from the previous two paragraphs: Since riming conditions appear above 2 km height and droplets formation conditions vanish aloft, liquid water starts to deplete along the vertical column at about 0830–0840 UTC. Then, roughly after 0930 UTC, the associated Doppler velocities (Fig. 9b) become smaller than 2 m s^{-1} (downwards). These magnitudes are typical fall velocities for unrimed snow and imply that most of the liquid water has been eliminated by this time. This is in agreement with the vanishing of liquid water paths in Fig. 7c, and the disappearance of discernible liquid water in Fig. 8a.

4. Discussion and conclusions

Accretion and coalescence are other scenarios, in addition to the three discussed in Section 2, by which droplets can be depleted (Rogers and Yau, 1991, p.163). In the last

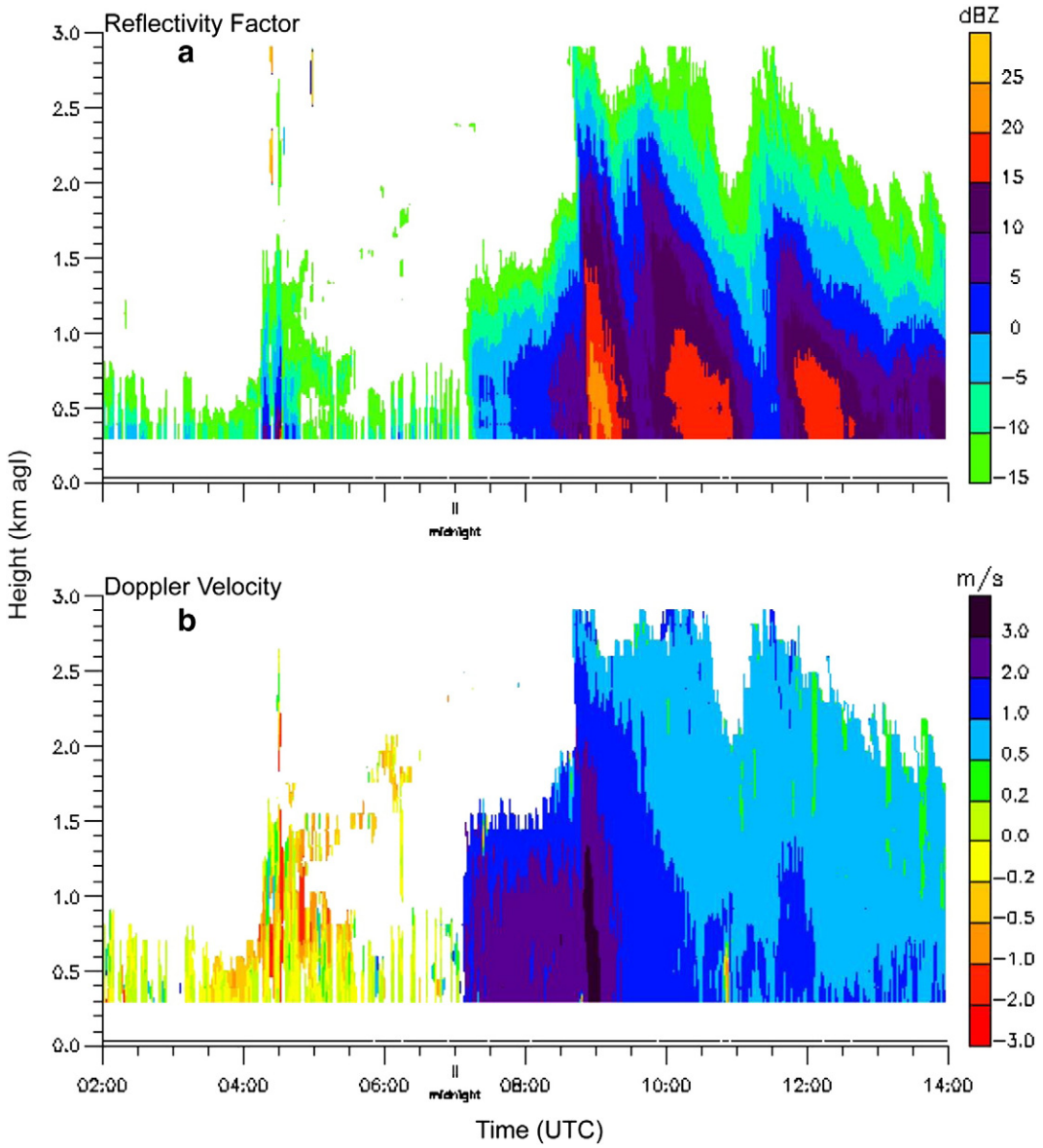

Fig. 9. UHF-band vertically-pointing radar observations of a winter upslope snowstorm (North-American Central High Plains) at Boulder, Colorado (USA), on 14 Feb 2008. Image courtesy of Dr. William Brown (NCAR, Earth Observing Laboratory).

paragraphs of Section 3.2, we noted that (after 0830 UTC) supercooled droplets were captured by snow particles during riming (i.e., accretion followed by freezing). The three scenarios discussed in Section 2.1—droplet-ice growth, evaporation deposition, and droplet-ice depletion—are most important during the earlier stages of cloud formation, whereas accretion and coalescence are most important during the mature stages of a precipitating cloud. The possibility of an advection scenario also exists, where cloud and precipitation particles—which originally evolved in a region with different conditions than those observed at the zenith—are transported (advected) into the sampling volume at a particular height.

Estimating the accuracy of radiometry estimates would require the comparison of radiometer retrievals with reference measurements that are currently unavailable. Radiosonde or aircraft observations (for example) are not adequate references for radiometer retrievals because these in-situ point measurements correspond to a volume of air much smaller than radiometer sampling volumes. Therefore, the differences between radiometer and radiosonde (or aircraft) observations do not imply errors in either the radiometer or the radiosonde. The reason is that radiosonde (point) and radiometer (volumetric) sensors never sample the same volume of air.

Similarly, because of the lack of a proper reference, the accuracy and skill of radiometry estimates for liquid water profiles remain unknown. Note also that dielectric properties of supercooled water are rather uncertain (Matzler et al., 2010), which introduces additional uncertainty about its

position in the cloud. Therefore, this work considers the radiometry detection of supercooled liquid water from a different perspective. The goal here is not to quantify the particularities of these retrieval errors. Instead, we aim to first identify and minimize the source of these errors and then to acknowledge the general terms of the retrieval errors. For example, consider that neural-network uncertainty and brightness-temperature measurement error contribute to the errors in temperature and vapor density retrievals (temperature and vapor density are used for computing e, e_s, and e_i, as in Section 2.1). We then have minimized the systematic errors by automated, continuous radiometer calibration (as explained previously), and minimized the random errors by training the neural-network algorithms with radiosonde observations that represent well the climatological conditions of each site (use of proper background data and vertical statistics is vital for achieving the highest accuracy). After that, we provide statistical confidence values to the scenarios defined in Section 2.1 (as in Fig. 1), in order to identify regions that are prone to have supercooled liquid water. Additionally, we present here a method to estimate the minimum detectability of cloud liquid water from radiometry (Fig. 2). The study results evidence qualitative consistency of our conceptual model with current microphysical concepts and with independent observations by vertically pointing radar and ceilometer.

In summary, this study shows how radiometer profiling can provide new insights to complex relationships between temperature, relative humidity, cloud liquid and ice contents, and vapor density during snowstorms. Monitoring these thermodynamic variables allows the identification of winter-storm regions with growth or depletion of ice particles and droplets. The radiometer data analyses were enhanced significantly when combined with complementary observations by vertically pointing radar and ceilometer. Future applications of these instrument and analysis techniques include the development of monitoring and short-term prediction (nowcasting) of supercooled cloud liquid water, which is hazardous condition for air and surface transportation, a weather modification opportunity, and a climate radiative-budget challenge.

Acknowledgments

This work was supported by the U.S. Department of Energy under Contract DE-AC02-06CH11357. Radiometer observations for the snowstorm on 14 February 2008 are part of the dataset continually collected at the Radiometrics Corporation facilities. Radiometer and radar observations for the snowstorm on 23 February 2006 are part of the dataset collected for the Canadian CloudSat Calipso Validation Project (C3VP), at Environment Canada. We thank Mr. Peter Rodriguez (from Environment Canada) for maintaining the C3VP database and making it available to us. Dr. Emil Constantinescu (from Argonne National Laboratory) kindly assisted us in the computation of cumulative probability distributions by kernel density estimators. We are indebted to Prof. Fréderic Fabry (from McGill University) for providing us with displays of the X-band radar data during the C3VP field campaigns. We are also grateful to Dr. William Brown (from NCAR-EOL) for providing Fig. 9. We express thanks to Dr. Alexei Korolev and another anonymous colleague (both from Environment Canada) for reviewing an early version of this manuscript.

The submitted manuscript has been created in part by U Chicago Argonne, LLC, as Operator of Argonne National Laboratory ("Argonne") under Contract No. DE-AC02-06CH11357 with the U.S. Department of Energy. The U.S. Government retains for itself, and others acting on its behalf, a paid-up, nonexclusive, irrevocable worldwide license in said article to reproduce, prepare derivative works, works, distribute copies to the public, and perform publicly and display publicly, by or on behalf of the Government.

Appendix A. Accuracy in retrievals by microwave profiling radiometers

In order to ensure optimum accuracy in radiometer retrievals, the 22–30 GHz receiver noise diodes were calibrated before taking all measurements in this work. For this, the radiometer used the precipitation-free atmosphere as a cold target. By observing the brightness temperature of the sky at several elevation angles in rapid succession, the profiling radiometer then computed an estimate of the 22–30 GHz noise-diode temperatures. Details of this calibration method are discussed by Han and Westwater (2000) and by Radiometrics (2013, p. 50). Similarly, the 51–59 GHz receiver noise diodes were calibrated beforehand, by using an external liquid nitrogen target (brightness temperature near 78 K) and an internal ambient target (brightness temperature near ambient temperature, placed inside the radiometer and external to the antenna/receiver system), according to the method presented by Radiometrics (2013, p. 51).

A liquid water film on a radiometer radome can generate artificially high values of brightness temperature. In order to minimize this error, the profiling radiometers used in this study have radomes coated with hydrophobic materials that cause liquid water to form beads, which are cleared from the radome by air flow from a blower. A printed circuit board (rain sensor, measuring conductivity across a grid of gold-plated conductors) is mounted next to the radome and serves as a wet-radiometer flag. Data reported in this paper include the wet flag.

As explained in Section 2.1, we use the radiometer retrievals of temperature and vapor density as input to determine the three scenarios of our conceptual model. Statistical comparisons with simultaneous radiosonde observations (Güldner and Spänkuch, 2001; Liljegren et al., 2005; Cimini et al., 2006a, 2006b, 2011) demonstrate that the root-mean-square differences in temperature and vapor density values are smaller than 1 °C and smaller than 1 g m^{-3}, respectively, for heights below 500 m, over all seasons and at various locations. These differences are smaller than the representativeness error inherent in (radiosonde) point measurements below 500 m height and are comparable above 500 m height (Ware et al., 2003, 2013; Knupp et al., 2009). Hewison (2007) analyzed radiometer covariance errors during clear and cloudy weather, finding that temperature and water vapor (expressed as the natural logarithm of specific humidity) uncertainties are smaller than 1 °C and 40%, respectively, up to 4 km height. Recent analyses of radiometer temperature and humidity sounding above the boundary layer (Sánchez et al., 2013) indicate that the observation errors are comparable to those

typically assigned to radiosonde soundings when they are assimilated into numerical weather prediction models.

We also use the radiometer retrieval of liquid water path to validate our conceptual model. Agreement is obtained if the vapor-pressure scenarios (as described in Section 2.1) coincide with time changes in liquid water path. Note that uncertainties exist in radiometer retrievals of liquid water path, which can theoretically limit the attainable accuracy to between 20 and 30 g m^{-2} (e.g., Turner, 2007).

References

Agee, E.M., Gilbert, S.R., 1989. An aircraft investigation of mesoscale convection over Lake Michigan during the 10 January 1984 cold air outbreak. J. Atmos. Sci. 46, 1877–1897.

Bergeron, T., 1935. On the physics of cloud and precipitation. Proceedings of the 5th UGGI Assembly, 2. International Union of Geodesy and Geophysics, Lisbon, pp. 156–178.

Botev, Z.I., Grotowski, J.F., Kroese, D.P., 2010. Kernel density estimation via diffusion. Ann. Stat. 38 (5), 2916–2957. http://dx.doi.org/10.1214/10-AOS799.

Cadeddu, M.P., Peckham, G.E., Gaffard, C., 2002. The vertical resolution of ground-based microwave radiometers analyzed through a multiresolution wavelet technique. IEEE Trans. Geosci. Remote Sens. 40 (3), 531–540. http://dx.doi.org/10.1109/TGRS.2002.1000313.

Cadeddu, M.P., Turner, D.D., Liljegren, J.C., 2009. A neural network for real-time retrievals of PWV and LWP from arctic millimeter-wave ground-based observations. IEEE Trans. Geosci. Remote Sens. 47 (7, part 1), 1887–1900. http://dx.doi.org/10.1109/TGRS.2009.2013205.

Cadeddu, M.P., Liljegren, J.C., Turner, D.D., 2013. The atmospheric radiation measurement (ARM) program network of microwave radiometers: instruments, data, retrievals. Atmos. Meas. Technol. 6, 2359–2372.

Candlish, L.M., Raddatz, R.L., Asplin, M.G., Barber, D.G., 2012. Atmospheric temperature and absolute humidity profiles over the Beaufort Sea and Amundsen Gulf from a microwave radiometer. J. Atmos. Ocean. Technol. 29, 1182–1201. http://dx.doi.org/10.1175/JTECH-D-10-05050.1.

Cimini, D., Hewison, T., Martin, L., 2006a. Comparison of brightness temperatures observed from ground-based microwave radiometers during TUC. Meteorol. Z. 15, 19–25. http://dx.doi.org/10.1127/0941-2948/2006/0096.

Cimini, D., Hewison, T., Martin, L., Güldner, J., Gaffard, C., Marzano, F., 2006b. Temperature and humidity profile retrievals from ground-based microwave radiometers during TUC. Meteorol. Z. 15, 45–56. http://dx.doi.org/10.1127/0941-2948/2006/0099.

Cimini, D., Westwater, E.R., Gasiewski, A.J., Klein, M., Leuski, V.Y., Liljegren, J.C., 2007. Ground-based millimeter- and submillimeter-wave observations of low vapor and liquid water contents. IEEE Trans. Geosci. Remote Sens. 45 (7), 2169–2180. http://dx.doi.org/10.1109/TGRS.2007.897450.

Cimini, D., Westwater, E., Gasiewski, A., 2010. Temperature and humidity profiling in the Arctic using ground-based millimeter-wave radiometry and 1DVAR. IEEE Trans. Geosci. Remote Sens. 40, 1381–1388. http://dx.doi.org/10.1109/TGRS.2009.2030500.

Cimini, D., Campos, E., Ware, R., Albers, S., Giuliani, G., Oreamuno, J., Joe, P., Koch, S., Cober, S., Westwater, E., 2011. Thermodynamic atmospheric profiling during the 2010 Winter Olympics using ground-based microwave radiometry. IEEE Trans. Geosci. Remote Sens. 49, 4959–4969. http://dx.doi.org/10.1109/TGRS.2011.2154337.

Cober, S., Isaac, G., Strapp, W., 2001. Characterizations of aircraft icing environments that include supercooled large drops. J. Appl. Meteorol. 40, 1984–2002.

Crewell, S., Ebell, K., Löhnert, U., Turner, D.D., 2009. Can liquid water be retrieved from passive microwave zenith observations? Geophys. Res. Lett. 36 (L06803). http://dx.doi.org/10.1029/2008GL036934.

Decker, M., Westwater, E., Guiraud, F., 1978. Experimental evaluation of ground-based microwave radiometer sensing of atmospheric temperature and water vapor profiles. 17, 1788–1795.

Dunn, L., 1987. Cold air damming by the front range of the Colorado Rockies and its relationship to locally heavy snows. Weather Forecast. 2, 177–189.

Ebell, K., Lohnert, U., Crewell, S., Turner, D., 2010. On characterizing the error in a remotely sensed liquid water content profile. Atmos. Res. 98, 57–68. http://dx.doi.org/10.1016/j.atmosres.2010.06.002.

Findeisen, W., 1938. Die kolloidmeteorologischen Vorgänge bei Neiderschlagsbildung (Colloidal meteorological processes in the formation of precipitation). Meteorol. Z. 55, 121–133.

Güldner, J., Spänkuch, D., 2001. Remote sensing of the thermodynamic state of the atmospheric boundary layer by ground-based microwave radiometry. J. Atmos. Ocean. Technol. 18, 925–933.

Gultepe, I., Pearson, G., Milbrandt, J., Hansen, B., Platnick, S., Taylor, P., Gordon, M., Oakley, J., Cober, S., 2009. The fog remote sensing and modeling field project. Bull. Am. Meteorol. Soc. 90 (3), 341–359.

Gunn, R., Kinzer, G., 1949. The terminal velocity of fall for water drops in stagnant air. J. Meteorol. 15, 243–248.

Han, Y., Westwater, E.R., 2000. Analysis and improvement of tipping calibration for ground-based microwave radiometers. IEEE Trans. Geosci. Remote Sens. 38 (3), 1260–1276. http://dx.doi.org/10.1109/36.843018.

Hewison, T.J., 2007. 1D-VAR retrieval of temperature and humidity profiles from a ground-based microwave radiometer. IEEE Trans. Geosci. Remote Sens. 45 (7), 2163–2168. http://dx.doi.org/10.1109/TGRS.2007.898091.

Hogg, D.C., Guiraud, F.O., Snider, J.B., Decker, M.T., Westwater, E.R., 1983. A steerable dual-channel microwave radiometer for measurement of water vapor and liquid in the troposphere. J. Clim. Appl. Meteorol. 22, 789–806.

Knupp, K., Ware, R., Cimini, D., Vandenberghe, F., Vivekanandan, J., Westwater, E., Coleman, T., Phillips, D., 2009. Ground-based passive microwave profiling during dynamic weather conditions. J. Atmos. Ocean. Technol. 26, 1057–1073. http://dx.doi.org/10.1175/2008JTECHA1150.1.

Korolev, A., 2007. Limitations of the Wegener–Bergeron–Findeisen mechanism in the evolution of mixed-phase clouds. J. Atmos. Sci. 64, 3372–3375.

Liljegren, J.C., Boukabara, S.A., Cady-Pereira, K., Clough, S.A., 2005. The effect of the half-width of the 22-GHz water vapor line on retrievals of temperature and water vapor profiles with a 12-channel microwave radiometer. IEEE Trans. Geosci. Remote Sens. 43 (5), 1102–1108. http://dx.doi.org/10.1109/TGRS.2004.839593.

Liu, A., Moore, W., 2004. Lake-effect snowstorms over Southern Ontario, Canada, and their associated synoptic-scale environment. Mon. Weather Rev. 132, 2595–2609.

Mahoney, J., Brown, J., Tollerud, E., 1995. Contrasting meteorological conditions associated with winter storms at Denver and Colorado Springs. Weather Forecast. 10, 246–260.

Matzler, C., Rosenkranz, P.W., Cermak, J., 2010. Microwave absorption of supercooled clouds and implications for the dielectric properties of water. J. Geophys. Res. 115, D23208. http://dx.doi.org/10.1029/2010JD014283.

Morrison, H., de Boer, G., Feingold, G., Harrington, J., Shupe, M.D., Sulia, K., 2012. Resilience of persistent Arctic mixed-phase clouds. Review Article. Nat. Geosci. 5, 11–17. http://dx.doi.org/10.1038/NGEO1332.

Murphy, D.M., Koop, T., 2005. Review of the vapour pressures of ice and supercooled water for atmospheric applications. Q. J. R. Meteorol. Soc. 131, 1539–1565. http://dx.doi.org/10.1256/qj.04.94.

Neter, J., Wasserman, W., Whitmore, G.A., 1988. Applied Statistics, Third edition. Allyn and Bacon, Boston0-205-10328-6 (1006 pp.).

Parsons, D., Dabberdt, W., Cole, H., Hock, T., Martin, C., Barrett, A.L., Miller, E., Spowart, M., Howard, M., Ecklund, W., Carter, D., Gage, K., Wilson, J., 1994. The integrated sounding system: description and preliminary observations from TOGA COARE. Bull. Am. Meteorol. Soc. 75, 553–567.

Press, W.H., Teukolsky, S.A., Vetterling, W.T., Flannery, B.P., 2002. Numerical Recipes in C: The Art of Scientific Computing, Second Edition Reprinted with Corrections. Cambridge University Press, New York.

Pruppacher, H., Klett, J., 1997. Microphysics of Clouds and Precipitation. (2nd rev. and enl. ed.) Kluwer Academic Publishers, The Netherlands.

Radiometrics, 2013. Profiler Operator's Manual, MP-3000A, MP-2500A, MP-1500A. Radiometrics Corporation, Boulder, CO, USA (62 pp.).

Raju, C.S., Renju, R., Antony, T., Mathew, N., Moorthy, K.K., 2013. Microwave radiometric observation of a waterspout over coastal Arabian Sea. IEEE Trans. Geosci. Remote Sens. 10 (5), 1075–1079. http://dx.doi.org/10.1109/LGRS.2012.2229960.

Rogers, R., Yau, M., 1991. A Short Course in Cloud Physics, 3rd ed. Pergamon Press, England.

Rosenkranz, P.W., 1998. Water vapor microwave continuum absorption: a comparison of measurements and models. Radio Sci. 33, 919–928.

Röttger, J., Larsen, M.F., 1990. UHF/VHF radar techniques for atmospheric research and wind profiler applications. In: Atlas, David (Ed.), Radar in Meteorology. American Meteorological Society, Boston, MA, USA, pp. 235–281.

Sánchez, J., Posada, R., García-Ortega, E., López, L., Marcos, J., 2013. A method to improve the accuracy of continuous measuring of vertical profiles of temperature and water vapor density by means of a ground-based microwave radiometer. Atmos. Res. 122, 43–54.

Serke, D., Hall, E., Bognar, J., Jordan, A., Abdo, S., Baker, K., Seitel, T., Nelson, M., Reehorst, A., Ware, R., McDonough, F., Politovich, M.K., (2014). Supercooled liquid water content profiling case studies with a new vibrating wire sonde compared to ground-based microwave radiometer. Atmos. Res. 149, 77–87.

Solheim, F., Godwin, J., Ware, R., 1998a. Passive ground-based remote sensing of atmospheric temperature, water vapor, and cloud liquid water profiles by a frequency synthesized microwave radiometer. Meteorol. Z. 7, 370–376.

Solheim, F., Godwin, J., Westwater, E., Han, Y., Keihm, S., Marsh, K., Ware, R., 1998b. Radiometric profiling of temperature, water vapor and cloud liquid water using various inversion methods. Radio Sci. 33, 393–404.

Tjernström, M., Sedlar, J., Shupe, M.D., 2008. How well do regional climate models reproduce radiation and clouds in the Arctic? An evaluation of ARCMIP simulations. J. Appl. Meteorol. Climatol. 47 (9), 2405–2422. http://dx.doi.org/10.1175/2008JAMC1845.1.

Turner, D.D., 2007. Improved ground-based liquid water path retrievals using a combined infrared and microwave approach. J. Geophys. Res. - Atmos. 112, D15204. http://dx.doi.org/10.1029/2007JD008530.

Ware, R., Carpenter, R., Güldner, J., Liljegren, J., Nehrkorn, T., Solheim, F., Vandenberghe, F., 2003. A multi-channel radiometric profiler of temperature, humidity and cloud liquid. Radio Sci. 38, 8032–8079. http://dx.doi.org/10.1029/2002RS002856.

Ware, R., Cimini, D., Campos, E., Giuliani, G., Albers, S., Nelson, M., Koch, S.E., Joe, P., Cober, S., 2013. Thermodynamic and liquid profiling during the 2010 Winter Olympics. Atmos. Res. 132–133, 278–290. http://dx.doi.org/10.1016/j.atmosres.2013.05.019.

Wegener, A., 1911. Thermodynamik der Atmosphäre. Barth, Leipzig (331 pp.).

Westwater, E.R., Han, Y., Solheim, F., 2000. Resolution and accuracy of a multi-frequency scanning radiometer for temperature profiling. In: Pampaloni, Paloscia (Eds.), Microwave Remote Sensing of the Earth's Surface and Atmosphere. VSP, pp. 129–135.

Xie, S., Boyle, J., Klein, S., Klein, S.A., Liu, X., Ghan, S., 2008. Simulations of Acrtic mixed-phase clouds in forecasts with CAM3 and AM2 for M-PACE. J. Geophys. Res. 113, D04211. http://dx.doi.org/10.1029/2007JD009225.

Xu, G., Ware, R., Zhang, W., Feng, G., Liao, K., Liu, Y., 2014. Effect of off-zenith observations on reducing the impact of precipitation on ground-based microwave radiometer measurement accuracy. Atmos. Res. 85–94. http://dx.doi.org/10.1016/j.atmosres.2014.01.021.

Xue, L., Hashimoto, A., Murakami, M., Rasmussen, R., Tessendorf, S., Breed, D., Parkinson, S., Holbrook, P., Blestrud, D., 2013a. Implementation of a silver iodide cloud-seeding parameterization in WRF. Part I: Model description and idealized 2D sensitivity tests. J. Appl. Meteorol. Climatol. 52, 1433–1457.

Xue, L., Hashimoto, A., Murakami, M., Rasmussen, R., Tessendorf, S., Breed, D., Parkinson, S., Holbrook, P., Blestrud, D., 2013b. Implementation of a silver iodide cloud-seeding parameterization in WRF. Part II: 3D simulations of actual seeding events and sensitivity tests. J. Appl. Meteorol. Climatol. 52, 1458–1476.

Zawadzki, I., Fabry, F., Szyrmer, W., 2001. Observations of supercooled water and secondary ice generation by a vertically pointing X-band Doppler radar. Atmos. Res. 59–60, 343–359.